PHYSICAL REVIEW E **104**, 045304 (2021)

Equilibrium properties of warm dense deuterium calculated by the wave packet molecular dynamics and density functional theory method

Yaroslav Lavrinenko,[1,2] Pavel R. Levashov,[1,2] Dmitry V. Minakov,[1,2] Igor V. Morozov,[1,2,*] and Ilya A. Valuev[1]
[1]*Joint Institute for High Temperatures of Russian Academy of Sciences, Moscow 125412, Russia*
[2]*Moscow Institute of Physics and Technology, Dolgoprudny 141701, Russia*

(Received 14 July 2021; accepted 13 September 2021; published 12 October 2021)

A joint simulation method based on the wave packet molecular dynamics and density functional theory (WPMD-DFT) is applied to study warm dense deuterium (nonideal deuterium plasmas). This method was developed recently as an extension of the wave packet molecular dynamics (WPMD) in which the equations of motion are solved simultaneously for classical ions and semiclassical electrons represented as Gaussian wave packets. Compared to the classical molecular dynamics and WPMD simulations, the method of WPMD-DFT provides a more accurate representation of quantum effects such as electron-ion coupling and electron degeneracy. It allows studying nonadiabatic dynamics of electrons and ions in equilibrium and nonequilibrium states while being more accurate and efficient at high densities than WPMD and classical molecular dynamics. In the paper, we discuss particular features of the method such as special boundary conditions and the procedure of isentrope calculation as well as the results obtained by WPMD-DFT for the shock-compressed deuterium. The compression isentrope and principal Hugoniot curves obtained by WPMD-DFT are compared with available experimental data and other simulation approaches to validate the method. It opens up a possibility of further application of the method to study nonequilibrium states and relaxation processes.

DOI: 10.1103/PhysRevE.104.045304

I. INTRODUCTION

A combination of the wave packet molecular dynamics (WPMD) simulation technique and the density functional theory (DFT) called WPMD-DFT was proposed recently [1,2]. The area of applicability of this new method includes equilibrium properties and dynamical (nonequilibrium) processes in electron-ion nonideal (strongly coupled) plasmas and warm dense matter such as the equation of state, electron-ion relaxation, electron and ion plasma waves, plasma conductivity, reflectivity, diffusion, etc. These properties are of importance in view of recent experiments with shock-compressed gases [3,4], laser ablation [5,6], and interaction of femtosecond laser pulses with nanoparticles [7–9].

The method of WPMD for simulations of nonideal electron-ion plasmas was developed in [10–12]. This method was meant as an extension of the classical molecular dynamics (MD) commonly used to study such systems [13–16]. In both MD and WPMD methods the electrons and ions are represented as particles for which the equations of motion are solved. As opposed to the Born-Oppenheimer approximation, where quantum electrons are treated statically, the full dynamical approach allows one to simulate nonadiabatic processes such as electron-ion relaxation [14,17], oscillation of electrons in nanoclusters [9,18], electron plasma waves [14,19], etc. Note that these methods should be distinguished from the molecular dynamics of atoms typical for simulations of simple molecules, liquids, solids, polymers, and biological systems where the electronic degree of freedom is incorporated in the interatomic interaction.

In the classical MD models for nonideal plasmas the interaction between particles, including electrons, is described mostly by the Coulomb potential corrected at short distances to account for quantum effects (see [20,21]). Thus, the classical MD requires the choice of a particular form of electron-ion and electron-electron pseudopotentials describing interaction at short distances. These pseudopotentials and their dependence on the thermodynamic temperature are often the subjects of debate.

The idea of WPMD is to replace pointlike electrons with Gaussian wave packets. The wave packet is a simple spatially localized form of a single electron wave function that depends on a small number of parameters. The WPMD approach relies more on first principles than the classical MD. For example, the effective electron-ion and electron-electron pseudopotentials are no longer required because electrons are treated as quantum particles. However, WPMD is less accurate in describing atoms and molecules than DFT or first-principles quantum chemistry. The variational freedom in the wave function expansion is very restricted in WPMD, as it is usually limited to eight parameters per electron. In its original formulation, the many-electron wave function in WPMD is given by the Hartree product so that exchange-correlation effects are missing as well. In fact, this is the price to pay for numerical efficiency and the ability to study nonadiabatic processes.

There are several simulation methods which may be regarded as extensions of the WPMD approach. In the method of electron force field (eFF) [22] the effective electron interactions (pseudopotentials) are reintroduced to tune the

---

[*] morozov@ihed.ras.ru

atomic bound state energies and to account for the electron exchange effects. In the antisymmetrized wave packet molecular dynamics (AWPMD) the many-body wave function for electrons with the same spin projection is antisymmetrized using the unrestricted Hartree-Fock approximation [23–25]. Another branch of WPMD methods uses the representation of a single electron wave function by multiple Gaussian wave packets which significantly improves the bound state energies [26–28]. All these modifications of the original WPMD approach except for eFF reduce the simulation performance significantly.

In [1,2] a new WPMD modification was proposed where a single Gaussian wave packet per electron and the Hartree approximation (nonantisymmetrized) for the many-electron wave function are used with a complementary term added to the system Hamiltonian to account for the electron exchange-correlation effects. This term is calculated as a functional of the electron density following the idea of DFT. In our case, the local electron density is obtained from the wave packet positions and widths. We call this method as WPMD-DFT. In this paper we discuss mainly the results obtained by this approach.

The calculation of the exchange-correlation term in WPMD-DFT reduces the simulation performance but not to the same extent as for AWPMD. Moreover, the calculation of the exchange-correlation functional can be efficiently parallelized on graphical processing units (GPUs) reducing the computation time by one or two orders of magnitude. At present our WPMD-DFT algorithm is implemented as a part of the open source code LAMMPS [29].

Another feature of the present WPMD-DFT implementation is the use of reflecting boundary conditions [1,30] instead of the periodic boundaries typical in the classical MD simulations and WPMD. Reflecting boundaries solve the problem of the infinite wave packet spreading for weakly coupled electrons [31]. In this paper, we pay special attention to the influence of reflecting boundaries and the simulation box size on the obtained results.

The wave packet method allows creating of two types of algorithms: (i) molecular dynamics for studying nonequilibrium states, dynamic processes, and relaxation (WPMD-DFT); (ii) Monte Carlo for studying equilibrium systems using the Metropolis algorithm (WPMC-DFT). The results of WPMC-DFT simulations were reported in [1,2]. In this paper, we focus on the dynamical WPMD-DFT simulations.

We test our WPMD-DFT approach using experimental data on thermodynamic properties of warm dense hydrogen and deuterium. These substances have recently been a subject of application and benchmarking for many quantum simulation methods. On the one hand, dense hydrogen and deuterium are very interesting from the theoretical point of view because of the effects of Coulomb interaction and degeneracy. On the other hand, hydrogen is the most widespread element in the Universe that determines the features of different astrophysical objects. That is why the experimental investigation of warm dense hydrogen and deuterium draws a lot of attention during the last decades. Shock compression of solid and liquid deuterium [32–37], hydrogen and deuterium metallization [38–42], and quasi-isentropic compression [43–47] has been actively investigated by many researchers.

The state of electrons which is both quantum degenerate and electrostatically strongly coupled requires a simulation model that accounts for the Pauli exclusion principle and a treatment of the Coulomb interaction at small interparticle separations. The most rigorous and *ab initio* model in this field is path integral Monte Carlo (PIMC) [48,49]. The limitations of PIMC are large temperature and small number of particles. Quantum molecular dynamics (QMD) based on DFT with a plane wave basis can be applied to simulate the ion dynamics in frames of the Born-Oppenheimer approximation for electrons. The DFT method with the plane wave expansion is the most used QMD technique for simulation of warm dense matter, however it is limited to small temperatures. Orbital-free DFT (OFDFT) approaches [50] extend to higher temperatures while compromising the accuracy of electronic orbitals description. Time-dependent versions of both DFT [51] and orbital-free DFT [52] go beyond the Born-Oppenheimer approximation for the electrons and treat the electrons dynamically. In contrast to WPMD, which incorporates electron dynamics intrinsically, in time-dependent DFT the dynamics started from the single-determinant eigenstate wave function requires additional coupling terms.

Numerous computational works are devoted to the hypothetical plasma phase transition or liquid-liquid phase transition in dense deuterium [53–58]. While for more complicated substances only DFT-based approaches can be applied, a variety of Monte Carlo methods are widely used for hydrogen and deuterium simulations, in particular, path integral Monte Carlo (PIMC) at relatively high temperatures [48,49] and quantum Monte Carlo (QMC) at low temperatures [56,59].

WPMD in its original formulation [11] and WPMD with antisymmetrization of electrons (AWPMD) [23] were involved in the simulations of deuterium shock Hugoniot and dissociative phase transition and showed only qualitative agreement with experiments and more accurate methods [24]. Therefore, the original WPMD and AWPMD methods turned out to be not practical without serious improvements. In this work, we demonstrate that our modification, WPMD-DFT, provides much better agreement with recent experiments on shock and quasi-isentropic compression of hydrogen and deuterium. Special attention is paid to the unique experimental achievements at pressures higher than 100 Mbar [46]. Aside from WPMD-DFT we calculate the compression isentrope of deuterium using the quantum molecular dynamics (QMD) method. The results given below show that the method of WPMD-DFT provides reasonable accuracy for thermodynamic properties at moderate and high temperatures being capable of simulating dynamic processes in strongly coupled quantum systems. The ability to study nonequilibrium processes was confirmed in [1] by simulations of electron-ion relaxation.

In Sec. II we briefly describe the method of WPMD-DFT. A simple evaluation of the accuracy of the method is performed by comparing the ground state energies of the hydrogen atom and molecule with the original WPMD calculations and experimental values. The results obtained by WPMD-DFT and WPMC-DFT are presented in Secs. III and IV. In Sec. III we analyze simulations of the deuterium plasma at the maximal densities available in experiments.

The influence of boundary conditions is discussed and a special algorithm is proposed to interpret simulation results in the case of reflecting boundaries. The deuterium isentrope obtained by different WPMD-DFT simulation procedures is compared with QMD calculations and experiments. We also evaluate WPMD-DFT and QMD performances for these particular simulations. In Sec. IV we discuss the Hugoniot curve of shock compressed hydrogen which has been studied for several decades. The WPMD-DFT results are evaluated with respect to other simulation approaches and experimental data. Conclusions and outlook are given in Sec. V.

II. SIMULATION METHOD

A. Basics of the WPMD-DFT simulation algorithm

The details of WPMD method are described in [11,24,25]; here we briefly mention its main principles. In this method the ions are treated as classical pointlike particles and a single-electron wave function is represented as a normalized Gaussian wave packet [10] described by a set of eight scalar parameters: the wave packet position **r**, width *s*, and their conjugate momenta **p**, p_s:

$$\varphi(\mathbf{x}) = \left(\frac{3}{2\pi s^2}\right)^{3/4} \exp\left\{ -\left(\frac{3}{4s^2} - \frac{\mathrm{i}p_s}{2\hbar s}\right)(\mathbf{x}-\mathbf{r})^2 + \frac{i}{\hbar}\mathbf{p}\cdot(\mathbf{x}-\mathbf{r})\right\}. \tag{1}$$

Each quantum mechanical variable enters the quantum Hamiltonian together with its conjugate (momentum) counterpart, so the variable p_s is the conjugate for the width s. As seen from the time evolution equations below, p_s enters the wave packet definition in the way allowing one to interpret it as the rate of change of the wave packet width.

Within the Hartree approximation a many-body wave function is given as a product of the single-electron wave functions

$$\Psi(\{\mathbf{x}_k\}) = \prod_{k=1}^{N_\mathrm{e}} \varphi(\mathbf{x}_k), \tag{2}$$

where N_e is the number of electrons.

The resulting equations of time evolution for the wave packet parameters follow from the variational principle. They resemble the classical equations of motion in the fact that they may be derived from the generalized Hamiltonian function, which is the quantum expectation value of the system energy

$$\begin{aligned}
\hat{H}_\mathrm{WPMD} &= \sum_{k=1}^{N_\mathrm{e}} \frac{\hat{\mathbf{p}}_k^2}{2m_\mathrm{e}} + \sum_{k<l}^{N_\mathrm{e},N_\mathrm{e}} \frac{e^2}{|\hat{\mathbf{r}}_k - \hat{\mathbf{r}}_l|} \\
&\quad - \sum_{k,l}^{N_\mathrm{e},N_\mathrm{i}} \frac{Z_l e^2}{|\hat{\mathbf{r}}_k - \mathbf{R}_l|} + K_\mathrm{i} + U_\mathrm{ii} + \hat{U}_\mathrm{ext}, \\
H_\mathrm{WPMD} &= \langle\Psi|\hat{H}_\mathrm{wpmd}|\Psi\rangle \\
&= \sum_{k=1}^{N_\mathrm{e}} \left(\frac{\mathbf{p}_k^2}{2m_\mathrm{e}} + \frac{p_{sk}^2}{2m_\mathrm{e}} + \frac{9\hbar^2}{8m_\mathrm{e}s_k^2} - E_{0k}\right) \\
&\quad + \sum_{k<l}^{N_\mathrm{e},N_\mathrm{e}} \frac{e^2}{|\mathbf{r}_k - \mathbf{r}_l|} \operatorname{erf}\left(\frac{\sqrt{3}|\mathbf{r}_k - \mathbf{r}_l|}{\sqrt{2}(s_k^2 + s_l^2)^{1/2}}\right) \\
&\quad - \sum_{k,l}^{N_\mathrm{e},N_\mathrm{i}} \frac{Z_l e^2}{|\mathbf{r}_k - \mathbf{R}_l|} \operatorname{erf}\left(\frac{\sqrt{3}|\mathbf{r}_k - \mathbf{R}_l|}{\sqrt{2}s_k}\right) \\
&\quad + \sum_{k=1}^{N_\mathrm{i}} \frac{\mathbf{p}_{\mathrm{i}k}^2}{2m_\mathrm{i}} + \sum_{k<l}^{N_\mathrm{i},N_\mathrm{i}} \frac{Z_k Z_l e^2}{|\mathbf{R}_k - \mathbf{R}_l|} + U_\mathrm{ext},
\end{aligned} \tag{3}$$

where m_e and e are the electron mass and charge, m_i and Z_k are the ion mass and charge, $\mathbf{R}_k$ and $p_{\mathrm{i}k}$ are the ion position and momentum, N_i is the number of ions, K_i is the kinetic energy of ions, U_ii is the Coulomb energy of ion-ion interaction, and U_ext is an external energy related, for instance, to the boundary conditions (see below).

The idea of WPMD-DFT extension [1,2] is to use an additional energy term to account for exchange and correlation effects

$$H_\text{WPMD-DFT} = H_\mathrm{WPMD} + E_\mathrm{a}[n], \tag{4}$$

where $n = n(\mathbf{r})$ is the total electron density. In WPMD the density can be evaluated as a sum of the wave packet norms

$$n(\mathbf{r}) = \sum_{k=1}^{N_\mathrm{e}} \varphi_k(\mathbf{r})\varphi_k^*(\mathbf{r}). \tag{5}$$

The expression for E_a contains terms that describe exchange and correlation energy in the local density approximation, specific for WPMD,

$$E_\mathrm{a}[n] = \left(T_\mathrm{s}[n] - \sum_i T_\mathrm{s}[n_i]\right) + \left(E_\mathrm{XC}[n] - \sum_i E_\mathrm{XC}[n_i]\right), \tag{6}$$

where $n_i = \varphi_i(\vec{r})\varphi_i^*(\vec{r})$ is the electron density contribution from *i*th packet.

Note that for the Hartree approximation the single-electron wave functions in WPMD do not represent the eigenstates of the one-electron Hamiltonian with the self-consistent field. Populating of eigenstates according to the Pauli exclusion principle and the spins of individual electrons can not be performed in the WPMD case as it is done in the traditional DFT. We use the following approximation for the exchange part of the kinetic energy: The first contribution to the exchange energy for WPMD-DFT is the kinetic energy term $(T_\mathrm{s}[n] - \sum_i T_\mathrm{s}[n_i])$, where $T_\mathrm{s}[n]$ is the kinetic energy of the electron gas at zero temperature.

In WPMD-DFT this term is evaluated in the local density approximation first for the total electron density. Then the sum of kinetic energies of single wave packets evaluated over partial electronic densities is subtracted to maintain zero exchange energy for the limit of noninteracting electrons. The same approach is used for the electrostatic part of the exchange and correlation energy E_XC. It is evaluated over the total density and then the partial electronic contributions are subtracted.

The subtraction of partial electronic contributions from both the kinetic and electrostatic parts of the exchange-correlation energies can be treated as the general compensation for self-interaction and may be explained in the following way. In the traditional DFT, the exchange-correlation functionals E_{XC} include the exchange $E_{\mathrm{X}}[n]$ energy that is evaluated over the total electron density and already contains a compensation for the Coulomb self-interaction. In WPMD the Coulomb electron-electron interaction is introduced explicitly (3). Thus, no self-interaction compensation is needed for WPMD-DFT in $E_{\mathrm{X}}[n]$. To avoid double counting, the self-interaction term should be subtracted from the traditional DFT functionals when they are used in WPMD-DFT.

To compensate for double counting of self-interaction, in this work we employed the self-interaction correction approach from [60]. In WPMD-DFT the wave packet parameters are known and it is possible to evaluate the partial contributions of $E_{\mathrm{XC}}[n_{\mathrm{i}}]$ related to the ith packet. These contributions can be subtracted from the total energy $E_{\mathrm{XC}}[n]$ and it gives us the correct energy limit for a noninteracting system.

In the case of the self-interaction corrected LSDA approximation [60] used in this work we assign constant spin projection values to electrons (half of them have spin up and another half have spin down). Thus, the functionals have the form

$$E_{\mathrm{XC}}^{\mathrm{LSDA}}[n_\uparrow, n_\downarrow] = \int \epsilon_{\mathrm{XC}}(n_\uparrow, n_\downarrow) n(\mathbf{r})\, d\mathbf{r},$$

$$n(\mathbf{r}) = n_\uparrow(\mathbf{r}) + n_\downarrow(\mathbf{r}), \tag{7}$$

$$T_{\mathrm{s}}[n] = \frac{3}{10}(3\pi^2)^{2/3} \int n(\mathbf{r})^{5/3}\, d\mathbf{r}. \tag{8}$$

Analogously to simulations of classical systems, the equilibrium properties of the wave packet system may be obtained either by solving the equations of motion (WPMD) with time averaging or by sampling the phase space using the wave packet Monte Carlo (WPMC) method. The first method resembles the classical MD with additional degrees of freedom related to variation of wave packet widths

$$\dot{\mathbf{r}}_k = \frac{\partial H}{\partial \mathbf{p}_k}, \quad \dot{\mathbf{p}}_k = -\frac{\partial H}{\partial \mathbf{r}_k}, \quad \dot{s}_k = \frac{\partial H}{\partial p_{sk}}, \quad \dot{p}_{sk} = -\frac{\partial H}{\partial s_k}, \tag{9}$$

where H is given by (4). The partial derivatives at the right-hand sides of (9) may easily be obtained as analytical functions of the parameters $\mathbf{r}_k$, $\mathbf{p}_k$, s_k, p_{sk} and are calculated very efficiently for all components of H, except for E_{a}.

The Nosé-Hoover thermostat is used to equilibrate the system at a given temperature T. Since wave packet degrees of freedom describe electrons, the WPMD method incorporates the electron dynamics intrinsically. The WPMD method allows to obtain the temporal evolution of both electrons and ions so that it is suitable to study nonequilibrium states and relaxation processes.

The derivative of the E_{a} over a wave packet parameter $q \in (\mathbf{r}_k,\ s_k,\ \mathbf{p}_k,\ p_{sk})$ is evaluated using the mesh values of $T_{\mathrm{s}}[n]$ and $E_{\mathrm{XC}}[n]$ as

$$\frac{\partial E_{\mathrm{a}}}{\partial q} = \left(\frac{\partial T_{\mathrm{s}}[n]}{\partial n} + \frac{\partial E_{\mathrm{XC}}[n]}{\partial n} \right) \frac{\partial n}{\partial q}. \tag{10}$$

For WPMC simulations we use the Monte Carlo sampling varying the positions of ions $\mathbf{R}_k$ and all parameters of the wave packets $(\mathbf{r}_k, s_k, \mathbf{p}_k, p_{sk})$. Adaptive steps are used to keep the mean Monte Carlo acceptance rate at $\frac{1}{2}$. The ionic kinetic energy is decoupled and assumed to be equal to $(3/2)N_{\mathrm{i}}k_{\mathrm{B}}T$. The correction $N_{\mathrm{e}}k_{\mathrm{B}}T$ for extra degrees of freedom is subtracted from the obtained equilibrium energies.

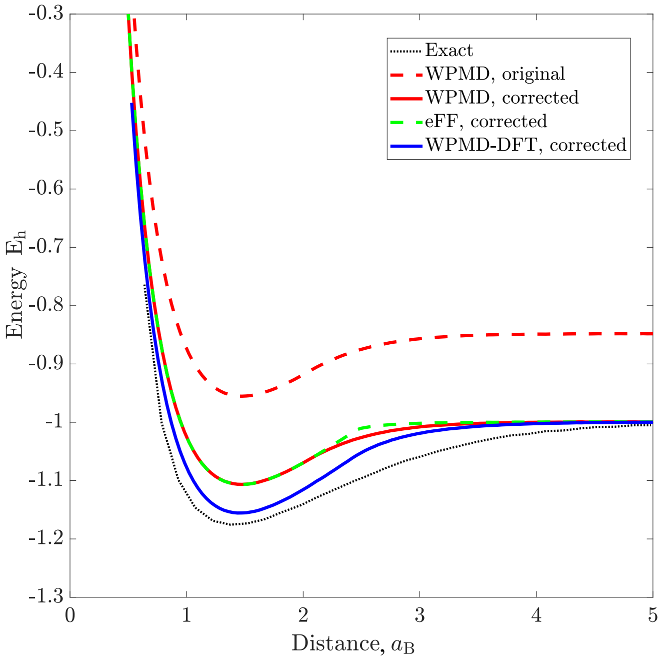

FIG. 1. Binding energy of the H_2 molecule depending on the bond length as obtained by simulations using the original WPMD algorithm (upper dashed red line), the same with corrected energy of isolated two-atom state (upper solid red line), the eFF method with correction (lower dashed green line), and WPMD-DFT with correction (lower solid blue line). The exact value is given by the black dotted line.

B. Ground states of the hydrogen atom and molecule

In order to demonstrate the effect of the exchange-correlation term in WPMD-DFT let us consider simple systems such as the hydrogen atom and molecule. As the hydrogen atom has only one electron, its model is not affected by adding $E_{\mathrm{a}}[n]$. Thus, the single-Gaussian electron representation gives the ground state energy of $-0.424\ E_{\mathrm{h}}$, known from the original WPMD simulations [11], which is lower than the exact value of $-0.5\ E_{\mathrm{h}}$ by 15% (E_{h} is the Hartree energy). This result can be improved by using multiple Gaussians per electron [26].

The binding energy for a two-atom system depending on the distance between the atoms for WPMD-DFT is shown in Fig. 1. For all methods shown a single Gaussian per electron was used so that at large distances the binding energy tends to the energy of a fully dissociated hydrogen molecule which exceeds the exact value by $2 \times (0.5–0.424) = 0.152\ E_{\mathrm{h}}$ due to the above-mentioned error of the single-atom representation (see the red curve). For all other curves we have subtracted this excess energy (they are marked as corrected).

The result shows that WPMD-DFT provides the best value of the hydrogen molecule dissociation energy that is $0.155\ E_{\mathrm{h}}$ compared to the exact value of $0.166\ E_{\mathrm{h}}$. The original WPMD and the electron force field (eFF) methods [22] result in

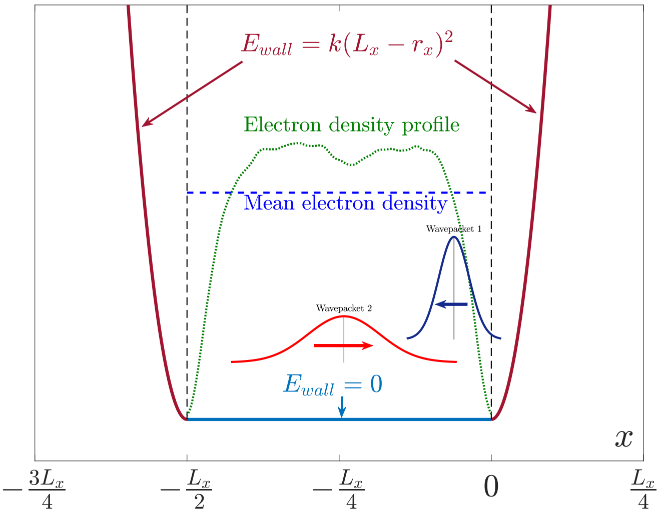

FIG. 2. The simulation box with a harmonic confining potential (dark red curves). The mean electron density for uniformly distributed electrons is shown by the blue dashed line, and the green dotted line is the sample of an actual electron profile obtained from simulations.

0.107 E_h. It shows the advantages of including the exchange-correlation term in WPMD-DFT.

As can be seen from Fig. 1 the hydrogen molecule bond length is well reproduced by all methods: 1.49 a_B for WPMD (in [10] the bond length for WPMD is reported as 1.47 a_B) and 1.47 a_B for WPMD-DFT. The exact value is 1.40 a_B.

C. Simulation of an extended system and calculation of pressure

One of the major problems of the original WPMD method is an unlimited broadening of the wave packets for weakly bound electrons. On the one hand, this broadening reflects the quantum nature of electrons and follows from the uncertainty relation. On the other hand, it constitutes a problem for the numerical algorithm. When a wave packet width reaches the size comparable to the simulation box length the corresponding electron ceases to interact with other particles and actually drops out of the simulation. While in a real system the electron wave function is limited by the interaction with borders, the periodic boundary conditions used typically for MD simulations correspond to a formally infinite system so that the wave packet widths are unlimited too.

There are few ways to overcome this problem (see [31]). The first of them was proposed in the original WPMD algorithm [12] where an additional harmonic term is introduced into the system Hamiltonian (3) $\Delta H = \sum_{k=1}^{N_e} (9\hbar^2 s_k^2)/(8m_e s_0^4)$; here s_0 is a parameter that limits the wave packet width. A similar approach is used in the eFF code [22]. As shown in [31] the value of s_0 can strongly affect the simulation results such as the collision frequency, plasma conductivity, etc.

In [30] it was proposed to replace the periodic boundaries by a confined system using a three-dimensional confining potential (wall potential) which not only keeps the particle positions within the simulation box but also restricts the wave packet widths (see Fig. 2)

$$U_{\text{wall}}(x) = \begin{cases} k(|x| - L/2)^2, & |x| > L/2 \\ 0, & |x| \leqslant L/2 \end{cases} \tag{11}$$

where $L = n_e^{-1/3} N_e$ is the simulation box edge. The wall parameter k determines the strength of the wall potential, acting on the wave packets and classical ions. This potential also disturbs the dynamics of wave packets but only in a small area close to the borders.

As shown in Fig. 2, on average the wave packet widths are smaller in the wall area than in the box center. Increasing the system size can reduce the boundary effects. In that sense, the influence of k is more controllable than the influence of the parameter s_0 so we prefer the use of the confining potential as a solution for the broadening problem. Moreover, a confined system is not fully artificial. It corresponds, for instance, to a cluster nanoplasma or the plasma in an electromagnetic trap.

A typical electron density profile along the x axis is shown in Fig. 2 by the green dotted line. It is calculated using the expression (5) and time averaging. The effect of boundary conditions is seen as a density drop near the boundary. Electron density profiles are discussed in more detail in Sec. III A.

Introducing of the reflecting walls causes other problems. If the value of k is too high (strong walls), it may lead to large forces on particles from the walls which destabilizes the time stepping. The low values of k (weak walls) do not keep the particles inside the box. This problem is discussed in more detail in Sec. III A.

At the same time, the use of reflecting boundaries has some advantages. In most MD simulations with periodic boundary conditions, the pressure is calculated via the virial expression from interparticle forces [16]. The confining potential (11) allows one to calculate the system pressure directly by evaluating the confinement forces F_α^{wall} acting on particles along each axis α,

$$P = \frac{1}{3}\left\langle \sum_{\alpha=x,y,z} \frac{|F_\alpha^{\text{wall}}|}{S_\alpha} \right\rangle, \tag{12}$$

where S_α is the area of the corresponding simulation box face. This method is free from assumptions used to obtain the pressure from the virial expression so that we used it in this work. As shown in [2] for low plasma densities and large system sizes these two methods give close results.

III. ISENTROPE OF HIGHLY COMPRESSED DEUTERIUM

As it was shown in [1,2] the original WPMD simulations fail at electron densities higher than 10^{22} cm^{-3}. It is seen from the drop of the internal energy and unphysical clustering of electrons inside the simulation box. Adding the exchange-correlation term extends the applicability of the method to much higher densities. In this paper we consider WPMD-DFT simulations for the densities up to 10^{25} cm^{-3}. To evaluate the results at high densities we refer to experimental studies of deuterium plasmas at megabar pressures generated by quasi-isentropic compression and to the corresponding QMD simulations.

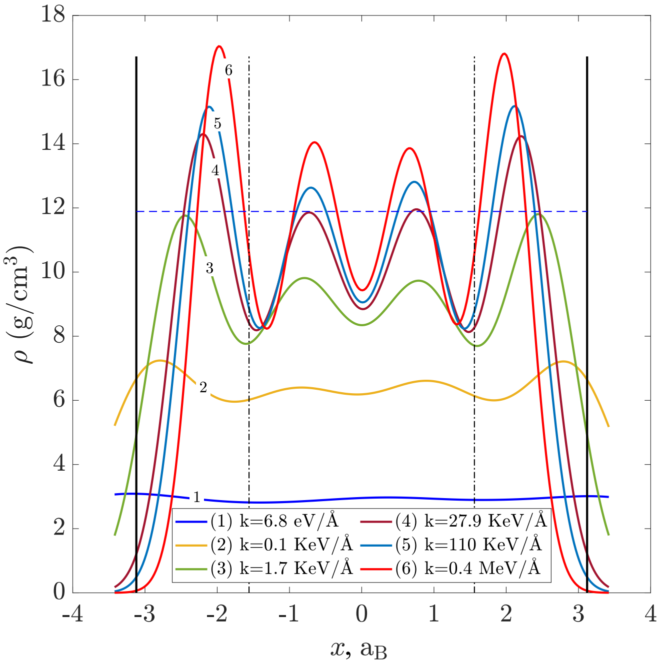

FIG. 3. The numbered solid lines show electron density profiles for different values of the wall parameter k (these values are given in the legend). The mean electron density of $\rho = 11.9$ g/cm^3 ($n_e = 3.55 \times 10^{24}$ cm^{-3}) is shown by the dashed line, the temperature is $T = 38\,240$ K. The solid vertical lines are located at the box boundaries $-L_x/2$ and $L_x/2$, the dotted-dashed lines outline the half-box region of $-L_x/4 < x < L_x/4$.

Performing WPMD-DFT simulations of the highly compressed deuterium plasma revealed two problems. One of them is caused by the special type of boundary conditions, the other one is related to the procedure of isentrope calculation. Both issues are discussed in the subsections below.

A. Influence of boundary conditions

As simulations show [1,2] the confining boundary conditions described in Sec. II allow us to solve the problem of wave packet broadening. Both the internal energy and the wave packet width distribution converge with the simulation box growth. Nevertheless, there arises nonuniformity of electron density profile within the simulation box (see Fig. 2).

Due to the reflections, the electron density has a peak in the box center and declines in the area close to the borders. Unlike classical particles, the wave packets interact with the wall before they cross it, and therefore the electron density in the vicinity of the box edge decreases. In contrast, the value of the electron density in the box center could be greater than the desired value of N_e/V where V is the simulation box volume excluding boundaries. Increasing the box size solves this problem at the cost of a substantial increase of the simulation time.

This problem becomes even more essential when considering very high plasma densities. In Fig. 3 the electron profiles are shown for the electron number density $n_e = 3.55 \times 10^{24}$ cm^{-3} and different values of the wall parameter k. One can see that for low values of k (weak boundaries) a large amount of the electron density is located outside the box so that the mean density within the box reduces significantly. With the increase of k the mean density returns to its normal value (dashed horizontal line) but the density becomes depleted near the walls. Periodic electron profile nonuniformities inside the box with the amplitude increasing with the increase of k indicate the formation of ordered structures (see Sec. IV). All these types of electron profile distortions affect the plasma properties obtained from simulations such as the pressure or correlation functions and therefore they should be taken into account.

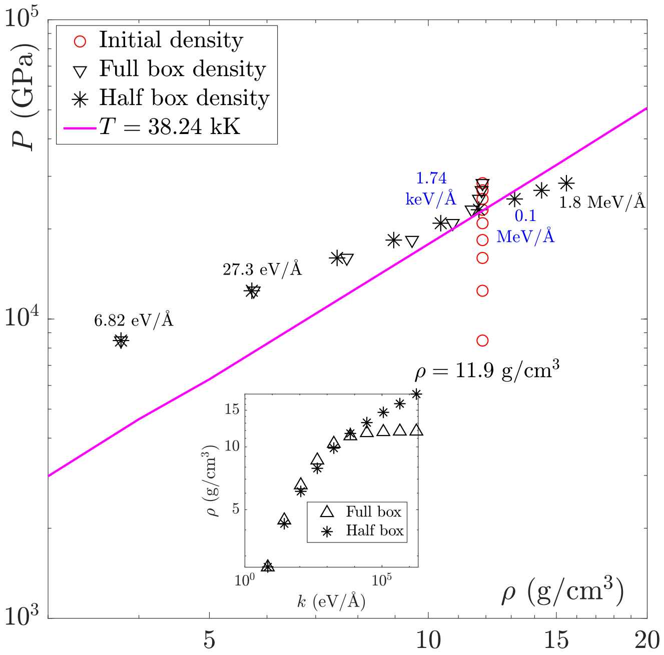

FIG. 4. The calculated values of pressure for different wall parameters k versus the number electron density calculated using there different ways: from the total number of electrons $n_e = N_e/V$ (circles), by integration of the actual electron profile over the full simulation box (13) (triangles), and by integration over the half-box (13) (asterisks). The deuterium plasma parameters are $\rho = 11.9$ g/cm^3 and $T = 38\,240$ K. The solid line represents the corresponding isotherm. The insertion shows the dependence of the mean electron density calculated using Eqs. (13) and (14) on the wall parameter k.

To illustrate the problem let us consider a fixed-size simulation box of the volume V filled with N_e electrons (wave packets). For the periodic boundary conditions the mean electron density is given by $n_e = N_e/V$. Using this value as a mean electron density for the confining boundary conditions gives rise to misleading results. The simulations show that the pressure P increases with the increase of k while the mean electron density n_e and the temperature T are constant (see the circles in Fig. 4). In other words, in this case the physical quantity P depends solely on the computational parameter k.

This problem originates from the fact that the value of $n_e = N_e/V$ is not related to the actual electron density profile formed in the simulation box. Alternatively, the mean electron density can be obtained as the integral over the full box

$$\langle n_e(\mathbf{r})\rangle_{V,\,t} = \frac{1}{V}\int_{-L_x/2}^{L_x/2}\int_{-L_y/2}^{L_y/2}\int_{-L_z/2}^{L_z/2} n(\mathbf{r})d\mathbf{r}, \qquad (13)$$

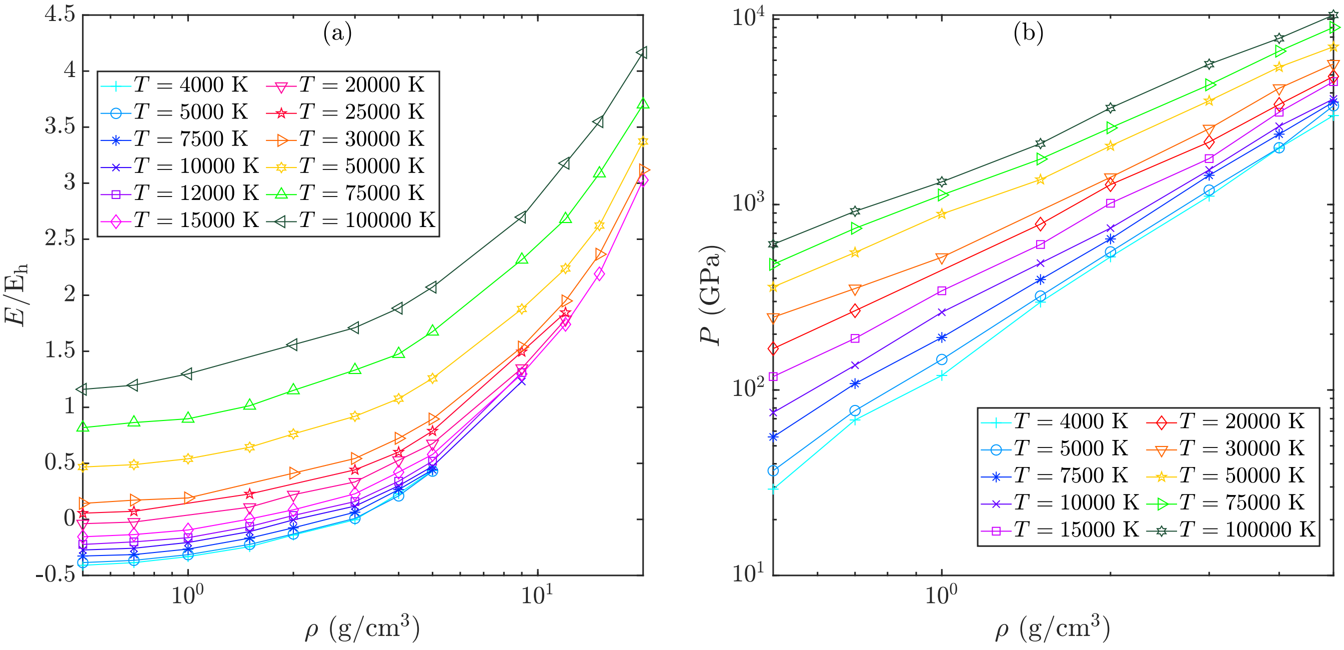

FIG. 5. Isotherms of deuterium obtained by WPMD-DFT: (a) internal energy, (b) pressure.

where $n(\mathbf{r})$ is defined in (5), and the index t means time averaging. The value of $\langle n_e(\mathbf{r})\rangle_{V,\,t}$ does not exceed n_e due to the exclusion of a part of electron density located outside the box.

Using the expression (13) as the mean electron density results in a more physically adequate dependence of P on the density (see the triangles in Fig. 4) which is close to the isotherm for $T = \text{const}$ except for the high values of k when the electron profile becomes strongly nonuniform. As the electron profile nonuniformities are located mainly near the walls the mean electron density can be calculated also as the integral over the half-box area located at the box center

$$\langle n_e(\mathbf{r})\rangle_{V/8,\,t} = \frac{8}{V}\int_{-L_x/4}^{L_x/4}\int_{-L_y/4}^{L_y/4}\int_{-L_z/4}^{L_z/4} n(\mathbf{r})d\mathbf{r}. \qquad (14)$$

This integration region is shown in Fig. 3 by dotted-dashed vertical lines.

As seen from the insertion in Fig. 4, for small values of k (weak walls) the results of (13) and (14) coincide indicating that the electron density is rather uniform (see also the lines 1 and 2 in Fig. 3). For large values of k (strong walls) the integration over that half-box (14) approximates the density more accurately as the increase of P could be explained by the corresponding increase of n_e (see asterisks in Fig. 4).

Based on these investigations for the simulations described below in this section we used the wall parameter of $k = 68$ keV/Å which is large enough to minimize the amount of electron density outside the box and small enough for the electron density profile to be rather uniform. The mean electron density is obtained using the integration over that half-box (14) that allows us to get reasonable results without a significant extension of the simulation box size.

B. Simulation of the isentropic compression

The calculation of a constant entropy curve (isentrope) from atomistic simulations can not be done straightforwardly. An extensive study of this problem can be found in [61] where four different ways to compute the collection of states with the same entropy are discussed. The most promising approaches for QMD calculations are successive Hugoniostat and isentropic integration. Earlier, we applied these two approaches to obtain release isentropes for aluminum and molybdenum using QMD [62]. Based on our experience [63,64] the isentropic integration method (also known as the Fermi-Zel'dovich approach) has proven to be the most convenient and precise.

In order to verify the WPMD-DFT algorithm we chose two different methods to obtain the deuterium isentrope. The first one is based on the Fermi-Zel'dovich approach when the following equation is solved to obtain an isentrope,

$$\left.\frac{dT}{dV}\right|_S = -T\left(\frac{\partial P}{\partial E}\right)_V, \qquad (15)$$

where $P(\rho, T)$ and $E(\rho, T)$ are the pressure and internal energy as functions of density and temperature.

This method requires the creation of a two-dimensional mesh for ρ and T and the calculation of mesh values for P and E. Each of the mesh points corresponds to an equilibrium system so that both WPMD-DFT and WPMC-DFT algorithms can be used. In Fig. 5 the mesh values are presented in the form of isotherms.

It is worth mentioning that Eq. (15) can be solved "on the fly" without using a previously computed mesh of values [61]. In this case, some finite-difference scheme is used as well as an estimator of the right-hand side of Eq. (15). However, the accuracy of such an approach depends on the volume increment and the error increases with the number of steps. To improve the accuracy one should carry out all calculations

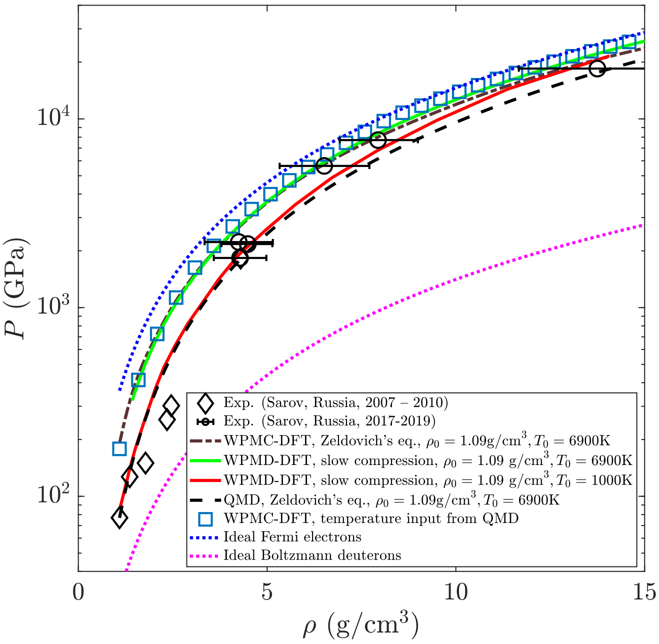

FIG. 6. Compression isentropes of deuterium in P-ρ plane obtained by two series of shock-compression experiments [43,44] (rhombus) and [46,65–67] (circles) as well as calculation results obtained by different methods: WPMC-DFT with the Fermi-Zel'dovich approach (brown dotted-dashed line), WPMD-DFT with the compression-relaxation algorithm started from different points (upper green and lower red solid lines), QMD with the Fermi-Zel'dovich approach (dashed black line), WPMC-DFT with density and temperature input from QMD (squares), ideal Fermi gas for electrons (upper blue dotted line), and ideal Boltzmann gas for deutrons (lower pink dotted line).

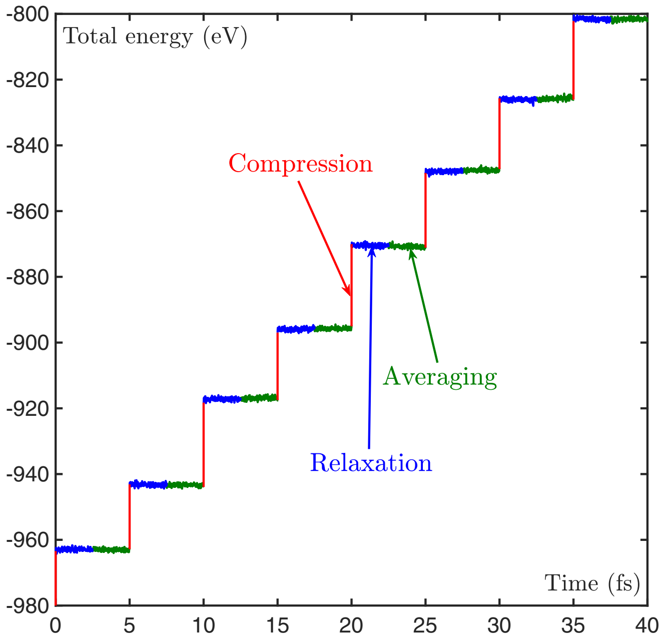

FIG. 7. Total energy of plasma as a function of time for the compression-relaxation algorithm of the isentrope calculation. Colors show the stages of compression, vertical red lines; relaxation, blue (dark gray) sections; and equilibrium states, green (light gray) sections.

again from the initial point. Moreover, any good estimator of the right-hand side of Eq. (15) is tedious in case of QMD simulations. On the other hand, a mesh of values can be refined so that previously computed points are not wasted.

In this work, to obtain an isentrope the functions $P(\rho, T)$ and $E(\rho, T)$ are interpolated with splines and Eq. (15) is solved numerically. The WPMD-DFT result for the starting point of $\rho = 1.09$ g/cm^3, $T = 6900$ K is shown in Fig. 6 by the purple line. The comparison with experimental points is given at the end of this section.

In the second method, the isentrope is calculated directly by compressing the plasma from a given initial state. This method is much faster as it requires the calculation of only a single WPMD-DFT trajectory instead of a bunch of trajectories in the Fermi-Zel'dovich approach. Its drawback is that the compression should be slow enough to ensure that the system passes through a series of equilibrium states.

Figure 7 illustrates the staircaselike compression algorithm. Each stair (should not be confused with the time step for the integration of the equations of motion which is much smaller) consists of three stages. The compression stage (red) means the sharp squeezing of the simulation box. It is followed by the relaxation stage (blue) where the equilibrium is restored. The equilibrium stage (green) is used for obtaining the plasma properties using time averaging.

The overall compression rate r is determined by the box squeezing ratio and the duration of each step. Figure 8 demonstrates how the compression rate affects the result for the isentrope calculation. The slower the compression, the closer the process to an equilibrium one. Simulations show that the result for $P(n_e)$ converges with the decrease of r and the relative error in determination of P does not exceed 13% for $r = 0.002$ Å/fs.

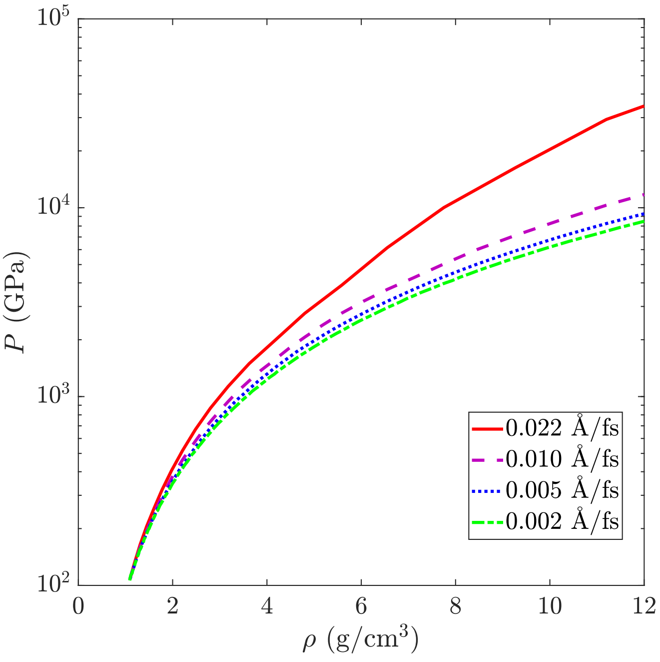

FIG. 8. Pressure as a function of the electron number density for different compression rates.

The results for the deuterium isentrope obtained by the compression-relaxation algorithm are shown in Fig. 6 by the green line for the starting point of $\rho = 1.09\ \mathrm{g/cm}^3$, $T = 6900$ K related to the QMD simulations (black dashed line) and by the red line for the starting point of $\rho = 1.09\ \mathrm{g/cm}^3$, $T = 1000$ K related to the experiment [43]. As can be seen, the first curve is very close to the Fermi-Zel'dovich approach with the same initial point which validates the compression-relaxation algorithm.

In addition to the two methods described above, we also performed WPMC-DFT simulations for a set of plasma densities and temperatures obtained from the QMD simulations (see squares in Fig. 6). The results agree well with the pure WPMD-DFT simulations using both the Fermi-Zel'dovich approach and the compression-relaxation algorithm provided that they start from the same initial point.

QMD simulations of the compression isentrope (black dashed line in Fig. 6) were performed using the VASP code [68]. The following parameters were used: The number of particles 64–256, one **k** point in the Brillouin zone, the cutoff energy for the plane waves varied from 600 to 1200 eV. All simulations were carried out in the canonical ensemble with the PAW pseudopotential [69] and PBE exchange-correlation functional [70]. The typical time step was 0.1 fs, the typical simulation time was about 10 ps.

Equation (15) was integrated numerically using the interpolation functions $P(\rho, T)$ and $E(\rho, T)$ calculated on the grid of isotherms and isochores. The initial point of the isentrope corresponds to the first experimental point from the paper [43] ($\rho_0 = 1.09\ \mathrm{g/cm}^3$, $P_0 = 77$ GPa), the temperature ($T_0 = 6900$ K) was fitted iteratively to satisfy the condition $P(\rho_0, T_0) = P_0$. In our earlier paper [63] we used 64 deuterium atoms so the temperature at the initial experimental point was 7600 K. In this work the number of atoms was increased up to 256, so the corrected value of $T_0 = 6900$ K was obtained in agreement with [71].

The deviation of the QMD isentrope from the experimental points at relatively low pressures [43] was discussed earlier [63,71]. However, the agreement with more recent experiments at pressures higher than 10^3 GPa (10 Mbar) and up to 1.8×10^4 GPa (180 Mbar) [44,46,67,72–74] is good. The experimental point at $P \approx 5500$ GPa published in [73,74] was recently corrected [67] and now agrees with the theoretical QMD curve.

The WPMC-DFT curve (squares in Fig. 6) calculated using the QMD temperatures as input parameters demonstrates higher pressures in comparison with the QMD simulations. The same is observed for the WPMC-DFT isentrope (green curve in Fig. 6) which originates from the initial point with the parameters $\rho_0 = 1.09\ \mathrm{g/cm}^3$, $T_0 = 6900$ K but at higher pressure than the experimental one. To obtain the experimental pressure of 77 GPa at the initial point, the temperature in the WPMD-DFT method should be about 1000 K. The corresponding isentrope (the red curve in Fig. 6) agrees well with all points at pressures higher than 10^3 GPa within the experimental error and is located slightly above the QMD isentrope. The dotted blue line shows the pressure of electron ideal Fermi gas confirming a strong influence of degeneracy effects along the compression curve.

TABLE I. Main parameters and comparative performances of WPMD-DFT and QMD codes for calculations of the equilibrium trajectories discussed in Sec. III B.

	QMD	WPMD-DFT
Simulation time step	10^{-16} s	10^{-18} s
Number of steps per trajectory	10^4–10^5	10^5–10^6
Model time per trajectory	1–10 ps	1 ps
Number of CPU cores or GPU units	64–128	6–8
Typical runtime	150 h	15 h
Runtime per step	9 s	0.09 s
Typical number of particles	64–256	256–512
Scaling with N	$O(N^3)$	$O(N)$–$O(N^2)$

C. Performance of WPMD-DFT and QMD simulations

The calculations considered in this section are good examples to compare performances of WPMD-DFT and QMD (DFT) algorithms. Optimizations and parallel efficiency of the WPMD-DFT code are discussed in [1,2]. This code is based on the LAMMPS parallel MD simulation package [29] (release No. 18, Sep 2018). The most time-consuming part of the algorithm related to the exchange-correlation energy is implemented for both CPUs (central processing units) and GPUs (graphics processing units) using NVidia CUDA environment. The parallel version of the code involves multiple GPUs with a single CPU thread per GPU. The benchmarks of the WPMD-DFT code were run on a hybrid computing cluster that includes Intel Xeon E5-2620 CPUs and NVidia GeForce GTX 1070 GPUs. The code was compiled by GCC 10.2 compiler.

The corresponding QMD simulations were performed using the VASP code [75], version 5.2. The code was compiled by Intel Fortran compiler (v. 17.0.2) and run on a pure CPU cluster that contained 64–128 Intel Xeon E5-2630v4 CPUs.

The typical parameters of QMD and WPMD-DFT simulations are presented in Table I. Note that in Table I we refer to the dynamical version of WPMD-DFT code (not the Monte Carlo sampling algorithm WPMC-DFT) which is more time consuming due to the calculation and space integration of the derivatives of the exchange-correlation term (10).

Although the codes were run in different environments, this table gives general information about their performances. One can see that the WPMD-DFT simulations can handle more particles and the scaling with the number of particles is much better. The typical runtimes and the runtime per step are 10–100 times smaller for WPMD-DFT. Therefore, in general the WPMD-DFT algorithm is faster than QMD for a single time step. On the other hand, explicit electron dynamics in WPMD-DFT requires time steps approximately 100 times smaller, so the total model times per trajectory for WPMD-DFT and the classical Born-Oppenheimer DFT appear to be comparable, whereas WPMD-DFT provides a much more detailed picture on the electron dynamics.

IV. DEUTERIUM SHOCK HUGONIOT

The WPMD-DFT method was applied to calculate the shock Hugoniot of deuterium. Shock-compression experiments are used to reconstruct the equation of state of matter for a given initial state with a known energy, pressure, and volume (E_0, P_0, v_0). The energy, pressure, and volume of the substance after shock compression are determined by the zeros of the Hugoniot function:

$$H(v,T) = E(v,T) - E_0 + \tfrac{1}{2}(v - v_0)[P(v,T) + P_0] = 0, \tag{16}$$

where v is the specific volume, $E(v,T)$ is the internal energy per atom, and $P(v,T)$ is the pressure.

In the calculations performed by the WPMD-DFT method, we used the initial state of deuterium with density $\rho = 0.167$ g/cm^3 and temperature $T = 22$ K. Such initial state was chosen for direct comparison with the experimental results presented in [32,35,36]. The selected parameters correspond to the pressure of $P_0 = 1.24 \times 10^{-4}$ GPa and the internal energy of $E_0 = -0.4996\ E_{\mathrm{h}}$/atom. The value of internal energy E_0 was obtained from WPMC-DFT simulation of an isolated D_2 molecule.

The Hugoniot curve was calculated for the temperature range of 2000 K $\leqslant T \leqslant$ 30 000 K and densities from $\rho = 0.167$ g/cm^3 $(n_e = 5 \times 10^{22}$ cm^{-3}, $r_s = [3/(4\pi n_e)]^{1/3} = 3.1821\ a_{\mathrm{B}})$ to $\rho = 1.67$ g/cm^3 $(n_e = 5 \times 10^{23}$ cm^{-3}, $r_s = 1.47\ a_{\mathrm{B}})$.

To obtain the points of the Hugoniot curve in the parameter range specified above, a set of molecular dynamics simulations by the WPMD-DFT method was performed. The result of each simulation was the pressure $P^{\mathrm{MD}}(v,T)$ and the energy $E^{\mathrm{MD}}(v,T)$ at a given specific volume v and temperature T. For the calculations, 10 isotherms and 10 isochores were selected to uniformly cover the region of interest. The obtained values were used to reconstruct the function $H(v,T)$, which was approximated by a quadratic polynomial depending on v at a fixed temperature T. The approximation was further used to solve the equation $H(v,T) = 0$ and determine the points of the shock Hugoniot.

Each WPMD simulation was organized in the following way. To obtain the points of the function $H(v,T)$, the deuterium plasma was simulated at the selected density n_e and temperature T. The simulated system consisted of 512 deuterium ions and 512 wave packets representing electrons. Wave packets were divided into two groups of 256 packets each with different spin projections $+\frac{1}{2}$ and $-\frac{1}{2}$. At the initial moment, the particles of the system were randomly and uniformly distributed in the volume determined by the density n_e, and were assigned random velocities corresponding to the Maxwellian distribution at a required temperature T. Then, 30 000 initial steps of molecular dynamics were performed with the time step of 0.001 fs with the Nosé-Hoover thermostat controlling the temperature. The thermostat ensured the initial equilibrium distribution of positions, velocities, and widths of the wave packets in the simulated system.

Then, 50 000 MD steps were performed with the same time step, but without using a thermostat. During this time, the energy and pressure were calculated, as well as their average values over all these time steps. If the initial value of the total energy differed from the final one by more than 1%, the thermostat was restarted and a new microcanonical ensemble was obtained. This made it possible to keep an error of the calculated observed values at the level of under 7% for pressure and $\lhd 1\%$ for energy. The low density and the selected values of the reflecting potential $k = 0.1$ KeV/Å made it possible to obtain a system with an average density in the central region close to the specified one, and thus no correction of the density (see Sec. III A) was needed for the Hugoniot simulations.

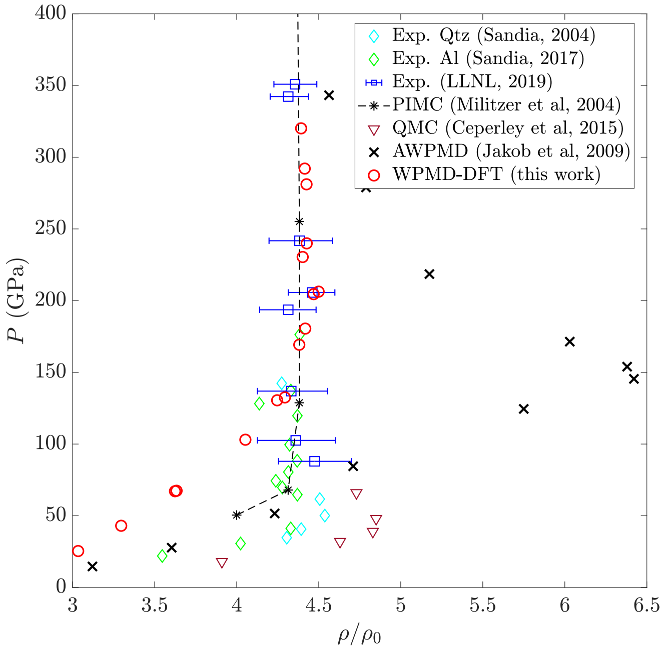

FIG. 9. Hugoniot curve of shock-compressed deuterium: experimental data from Sandia for the plate impact with α quartz [36] ("Expt. Qtz," cyan rhombus) and aluminum [35] ("Expt. Al," green rhombus) standards, experimental data from LNLL [37] (squares), PIMC simulations [77] (asterisks), QMC simulations [76] (triangles), AWPMD simulations [24] (crosses), and the present WPMD-DFT simulations (circles).

We compare the results of our calculations of the shock Hugoniot (Fig. 9 and Table II) with experimental data from [35–37] and the results of theoretical calculations by DFT [36], QMC [76], PIMC [77], and WPMD method with antisymmetrization [24].

TABLE II. WPMD-DFT simulations of the principal Hugoniot: compression, deuterium mass density, electron number density, temperature, and pressure (a limited set of states is presented); the states related to ion-ion pair-correlation functions in Fig. 10(a) and system snapshots in Fig. 11 are marked with bold.

ρ/ρ_0	ρ (g/cm^3)	n_{e} (10^{23}/cm^3)	T (K)	P (GPa)
3.03	**0.51**	**1.51**	**2000**	**25**
3.30	0.55	1.65	4000	43
3.63	**0.61**	**1.81**	**6000**	**67**
4.05	0.68	2.02	8000	103
4.29	**0.72**	**2.14**	**10000**	**133**
4.38	0.73	2.19	12000	169
4.47	0.75	2.23	14000	205
4.50	0.75	2.25	16000	206
4.40	**0.74**	**2.20**	**20000**	**230**
4.41	0.74	2.20	25000	292
4.39	0.73	2.19	30000	320

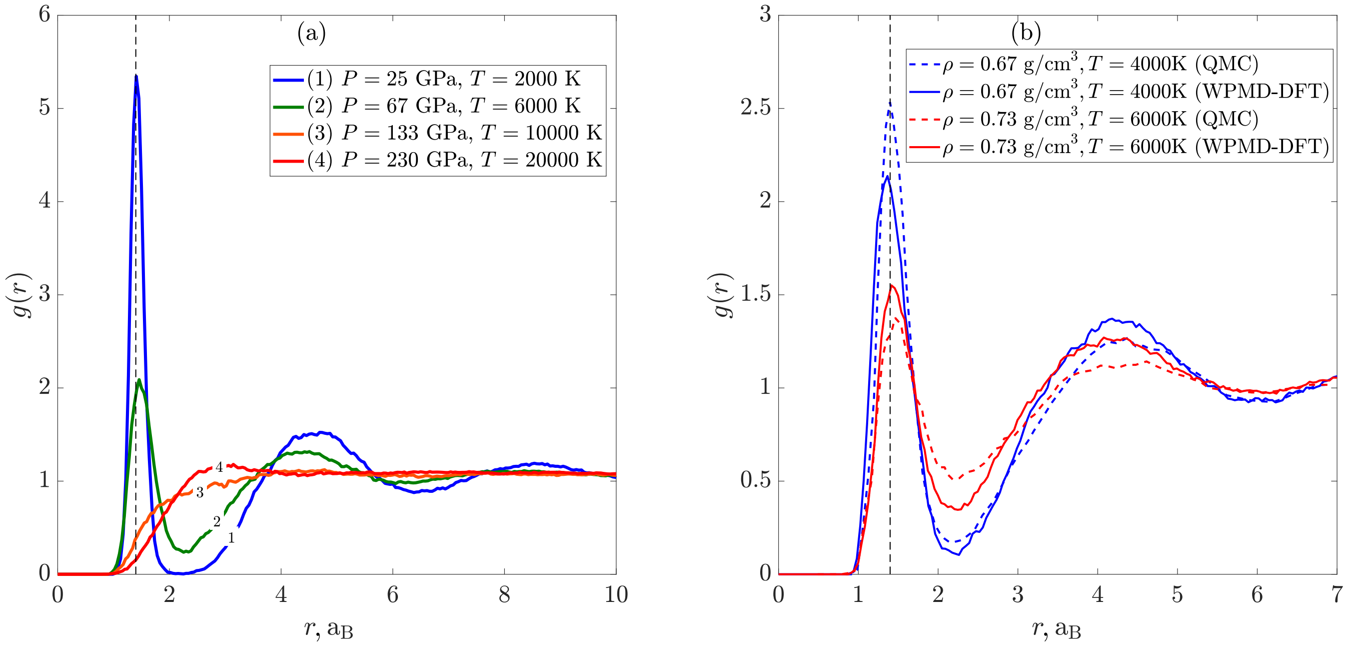

FIG. 10. Ion-ion pair correlation function for different densities and temperatures. The plasma parameters correspond to (a) selected points from the Hugoniout curve (see Fig. 9 and Table II); (b) the parameters of QMC simulations [76]. In (b) the solid lines are the present WPMD-DFT simulation, dashed lines are the results from [76].

The constructed shock Hugoniot shows the maximum values of the compression ratio $\rho/\rho_0 \approx 4.5$, which agrees with the experimental data from [36] to within 1%. The maximum compression value obtained by the AWPMD [11] method is 1.42 times higher than the experimental one. The QMC method gives 7% higher maximum compression value than that observed in the experiment. The PIMC method shows close results to the WPMD-DFT for the compression ratio.

A characteristic feature of the results obtained by WPMD-DFT is an overestimated pressure in the entire range of densities and temperatures which is similar to the calculations of deuterium isentrope (see Sec. III). Possible reasons for this are insufficient size of the system required to avoid the boundary effects associated with the reflective potential and the simple model of the electron wave function.

Also, the shock Hugoniot obtained by the WPMD-DFT method does not have a pronounced bend in the region close to the compressibility limit which is observed in experimental data and theoretical calculations by other methods, except for PIMC. A possible reason for this is the imperfection of the used exchange-correlation functional (LDA). The other theoretical calculations employ generalized gradient approximation (GGA) functionals. We expect the results to be more consistent in this region if GGA functionals are used instead of LDA.

In addition to the Hugoniot curve, pair-correlation functions of deuterium for selected points from the Hugoniot curve were calculated by the WPMD-DFT method [Fig. 10(a)]. We also compared pair-correlation functions obtained by the WPMD-DFT method with the data obtained by the QMC method [76] [Fig. 10(b)].

Figure 10(a) and the corresponding snapshots of the simulations box (Fig. 11) demonstrate the transition from the atomic to molecular states along the shock Hugoniot. The positions of the peaks in Fig. 10(a) coincide with the theoretical values corresponding to the interatomic distance in the deuterium molecule. It is seen that at $\rho = 0.51$ g/cm^3, $T = 2000$ K most of electrons are located in molecules. Moreover, the correlation function shows that the molecules are partially ordered so that the system is close to an amorphous state. The measured self-diffusion coefficient for ions in this state is 1.7×10^{-4} cm^2/s which is quite low but does not correspond to a molecular crystal. In the next snapshot at $\rho = 0.61$ g/cm^3, $T = 6000$ K the molecules are less ordered and the ionization rate increases which is visible by a larger number of free electrons and ionized molecules. For $\rho = 0.71$ g/cm^3, $T = 10\,000$ K the plasma state is reached with a small fraction of molecules. For $\rho = 0.74$ g/cm^3, $T = 20\,000$ K the system is fully ionized and disordered, the self-diffusion coefficient for ions in this state is 5×10^{-3} cm^2/s which is 30 times higher than at $T = 2000$ K.

The phase diagram of deuterium is discussed in various publications. In accordance with [57,58] the deuterium phase state at $P = 25$ GPa, $T = 2000$ K is a molecular liquid and the transition to an atomic liquid occurs roughly at $P = 50$ GPa, $T = 4000$ K. As one can see, the WPMD-DFT method slightly overestimates the transition temperature although a more comprehensive study is required to clarify this issue.

V. CONCLUSIONS

The WPMD-DFT method is applied for the calculations of thermodynamic properties of equilibrium systems. For both isentropic and shock compression of deuterium, the method is benchmarked against more accurate theoretical models (PIMC, QMD) and the experiment. The results are in a good agreement with both, except for overestimation of pressure.

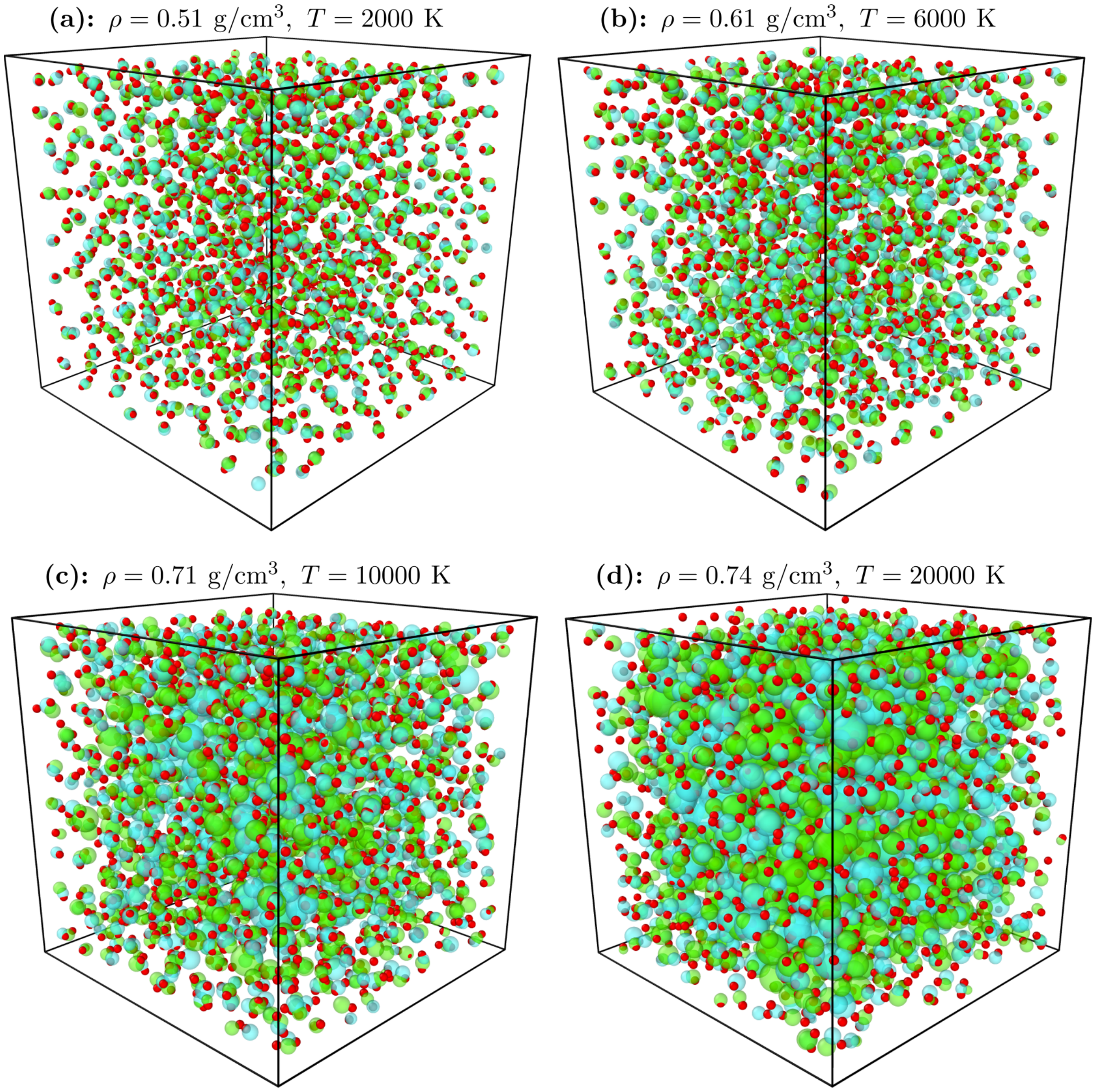

FIG. 11. Visualization of the simulation box for different plasma densities and temperatures. The plasma states correspond to Fig. 10(a) and Table II. Red spheres represent positions of ions, blue spheres are the electrons with the spin projection $\frac{1}{2}$, and green spheres are the electrons with the spin projection $-\frac{1}{2}$. The size of electron spheres corresponds to wave packet widths.

For the calculation of isentrope, a compression-relaxation algorithm is proposed for WPMD-DFT that is much faster than the solution of the Fermi-Zel'dovich's equation typically used in QMD. It is shown that these two algorithms give close results provided that the compression rate is slow enough.

In contrast to the previous AWPMD approach, the WPMD-DFT simulations result in the correct value for the deuterium compressibility on the principal Hugoniot curve. They describe the transition from molecular to atomic liquid, however, with some overestimation of the transition temperature and pressure.

The WPMD-DFT method is found to be more computationally efficient compared to the traditional plane wave DFT. It has no restrictions on the electron temperature, so its effectiveness relative to the plane wave DFT is higher for large temperatures.

Although this paper is concerned with simulations of equilibrium systems, the main purpose of WPMD-DFT is to study nonequilibrium states, dynamic and relaxation processes which makes this method rather universal. Verification of the method for equilibrium systems, presented in this work, opens up the possibility of applying it to simulations of conductivity, electron-ion relaxation, laser-plasma interaction, cluster nanoplasmas, etc. These topics are subjects for further work.

The WPMD-DFT method is one of the few computational techniques that describe, although qualitatively, the quantum dynamics of electrons in many-body systems. This opens up a possibility of extending this method to calculate various qualitative characteristics of plasma that enter higher level chemical or hydrodynamic models. At the same time, the WPMD-DFT method has a certain reserve for the increase of complexity and accuracy. For the typical model systems of up to 1024 particles, that are studied in this work, the dominant contribution to the total computational time is the grid-based calculation of the exchange and correlation energy $E_{\mathrm{a}}[n]$. This means that introduction of a more detailed description of the single-electron wave function, for example, multi-Gaussian expansion or higher momentum state wave packets, that affect only the basic Hamiltonian, would not lead to a significant increase in computational time. For larger systems (more than 10 K particles for the current WPMD-DFT) the $O(N)$-scaled grid-based $E_{\mathrm{a}}[n]$ computation would overperform the calculation of the Coulomb interaction in the basic Hamiltonian which is scaled as $O(N^2)$. In the following we discuss possible applications of the WPMD model extensions.

Degree of ionization is one of the important quantities that is expected to be calculated on the atomic level and to be provided to higher level chemical models. Separating electrons into free and bound ones in the microscopic model is a hard task with no strict guidelines to be used. The WPMD model adds an additional criterion to single out free electrons based on their width parameter. This criterion and the split-WPMD technique (multiple Gaussians) were applied earlier to simulate the excitation of the hydrogen atom by a high energy laser pulse [26].

Another issue that is left behind in this work is the application of WPMD-DFT for many-electron atoms and molecules. There are different approaches that can be used to handle multielectron atoms. In eFF, a suitable choice of the binding parameters allows one to simulate the elements of the second row of the periodic table. One of the problems here is the spherical symmetry of wave packets that can describe only the *s*-type states of the atoms. The difference is essential at lower temperatures where the binding energy and geometry strongly depend on the electron state. A more general DFT-like approach would include parametrized *p*- and *d*-type wave packets and the use of pseudopotentials to describe filled atomic shells.

ACKNOWLEDGMENTS

This work was supported by the Ministry of Science and Higher Education of the Russian Federation (Agreement with Joint Institute for High Temperatures RAS No. 075-15-2020-785). Computations were performed at the K-100 cluster (Keldysh Institute of Applied Mathematics RAS, Moscow), the Joint Supercomputer Center of RAS, and the JIHT RAS Supercomputer Centre. The authors also acknowledge the Shared Resource Centre “Far Eastern Computing Resource” IACP FEB RAS for providing computing time.

---

[1] Y. S. Lavrinenko, I. V. Morozov, and I. A. Valuev, Contrib. Plasma Phys. **59**, e201800179 (2019).

[2] Y. S. Lavrinenko, I. V. Morozov, and I. A. Valuev, J. Phys.: Conf. Ser. **1787**, 012043 (2021).

[3] Y. Zaporozhets, V. Mintsev, V. Fortov, H. Reinholz, G. Röpke, S. Rosmej, and Y. A. Omarbakiyeva, Phys. Rev. E **99**, 043202 (2019).

[4] Y. B. Zaporozhets, V. B. Mintsev, H. Reinholz, and G. Röpke, J. Phys.: Conf. Ser. **1787**, 012048 (2021).

[5] D. S. Sitnikov, J. Phys.: Conf. Ser. **1421**, 012001 (2019).

[6] M. E. Povarnitsyn and P. R. Levashov, Appl. Phys. A **125**, 688 (2019).

[7] P. Rupp, C. Burger, N. G. Kling, M. Kübel, S. Mitra, P. Rosenberger, T. Weatherby, N. Saito, J. Itatani, A. S. Alnaser *et al.*, Nat. Commun. **10**, 4655 (2019).

[8] R. G. Bystryi and I. V. Morozov, J. Phys. B: At., Mol. Opt. Phys. **48**, 015401 (2015).

[9] T. Raitza, G. Röpke, H. Reinholz, and I. Morozov, Phys. Rev. E **84**, 036406 (2011).

[10] D. Klakow, C. Toepffer, and P.-G. Reinhard, J. Chem. Phys. **101**, 10766 (1994).

[11] M. Knaup, P.-G. Reinhard, C. Toepffer, and G. Zwicknagel, J. Phys. A: Math. Gen. **36**, 6165 (2003).

[12] G. Zwicknagel and T. Pschiwul, J. Phys. A: Math. Gen. **39**, 4359 (2006).

[13] J. P. Hansen and I. R. McDonald, Phys. Rev. A **23**, 2041 (1981).

[14] I. V. Morozov and G. E. Norman, J. Exp. Theor. Phys. **100**, 370 (2005).

[15] I. Morozov, H. Reinholz, G. Röpke, A. Wierling, and G. Zwicknagel, Phys. Rev. E **71**, 066408 (2005).

[16] R. Bystryi, Y. Lavrinenko, A. Lankin, I. Morozov, G. Norman, and I. Saitov, High Temp. **52**, 475 (2014).

[17] L. X. Benedict, J. N. Glosli, D. F. Richards, F. H. Streitz, S. P. Hau-Riege, R. A. London, F. R. Graziani, M. S. Murillo, and J. F. Benage, Phys. Rev. Lett. **102**, 205004 (2009).

[18] M. Belkacem, F. Megi, P.-G. Reinhard, E. Suraud, and G. Zwicknagel, Eur. Phys. J. D **40**, 247 (2006).

[19] T. Pschiwul and G. Zwicknagel, J. Phys. A: Math. Gen. **36**, 6251 (2003).

[20] C. Deutsch, M. M. Gombert, and H. Minoo, Phys. Lett. A **66**, 381 (1978).

[21] A. V. Filinov, M. Bonitz, and W. Ebeling, J. Phys. A: Math. Gen. **36**, 5957 (2003).

[22] J. T. Su and W. A. Goddard, III, Phys. Rev. Lett. **99**, 185003 (2007).

[23] B. Jakob, P.-G. Reinhard, C. Toepffer, and G. Zwicknagel, Phys. Rev. E **76**, 036406 (2007).

[24] B. Jakob, P.-G. Reinhard, C. Toepffer, and G. Zwicknagel, J. Phys. A: Math. Theor. **42**, 214055 (2009).

[25] I. A. Valuev and I. V. Morozov, J. Phys.: Conf. Ser. **653**, 012153 (2015).

[26] I. V. Morozov and I. A. Valuev, Contrib. Plasma Phys. **52**, 140 (2012).

[27] P. E. Grabowski, A. Markmann, I. V. Morozov, I. A. Valuev, C. A. Fichtl, D. F. Richards, V. S. Batista, F. R. Graziani, and M. S. Murillo, Phys. Rev. E **87**, 063104 (2013).

[28] W. A. Angermeier and T. G. White, Plasma **4**, 294 (2021).

[29] S. J. Plimpton, J. Comput. Phys. **117**, 1 (1995).

[30] Y. S. Lavrinenko, I. V. Morozov, and I. A. Valuev, Contrib. Plasma Phys. **56**, 448 (2016).

[31] I. V. Morozov and I. A. Valuev, J. Phys. A: Math. Theor. **42**, 214044 (2009).

[32] W. J. Nellis, A. C. Mitchell, M. Van Thiel, G. J. Devine, R. J. Trainor, and N. Brown, J. Chem. Phys. **79**, 1480 (1983).

[33] G. W. Collins, L. B. Da Silva, P. Celliers, D. M. Gold, M. E. Foord, R. J. Wallace, A. Ng, S. V. Weber, K. S. Budil, and R. Cauble, Science **281**, 1178 (1998).

[34] G. V. Boriskov, A. I. Bykov, R. Il'kaev, V. D. Selemir, G. V. Simakov, R. F. Trunin, V. D. Urlin, A. N. Shuikin, and W. J. Nellis, Phys. Rev. B **71**, 092104 (2005).

[35] M. D. Knudson, D. L. Hanson, J. E. Bailey, C. A. Hall, J. R. Asay, and C. Deeney, Phys. Rev. B **69**, 144209 (2004).

[36] M. D. Knudson and M. P. Desjarlais, Phys. Rev. Lett. **118**, 035501 (2017).

[37] A. Fernandez-Panella, M. Millot, D. E. Fratanduono, M. P. Desjarlais, S. Hamel, M. C. Marshall, D. J. Erskine, P. A. Sterne, S. Haan, T. R. Boehly, G. W. Collins, J. H. Eggert, and P. M. Celliers, Phys. Rev. Lett. **122**, 255702 (2019).

[38] W. J. Nellis, A. C. Mitchell, P. C. McCandless, D. J. Erskine, and S. T. Weir, Phys. Rev. Lett. **68**, 2937 (1992).

[39] V. Y. Ternovoi, A. S. Filimonov, V. E. Fortov, S. V. Kvitov, D. N. Nikolaev, and A. A. Pyalling, Phys. B (Amsterdam) **265**, 6 (1999).

[40] M. D. Knudson, M. P. Desjarlais, A. Becker, R. W. Lemke, K. R. Cochrane, M. E. Savage, D. E. Bliss, T. R. Mattsson, and R. Redmer, Science **348**, 1455 (2015).

[41] R. P. Dias and I. F. Silvera, Science **355**, 715 (2017).

[42] P. M. Celliers, M. Millot, S. Brygoo, R. S. McWilliams, D. E. Fratanduono, J. R. Rygg, A. F. Goncharov, P. Loubeyre, J. H. Eggert, J. L. Peterson *et al.*, Science **361**, 677 (2018).

[43] V. E. Fortov, R. I. Ilkaev, V. A. Arinin, V. V. Burtzev, V. A. Golubev, I. L. Iosilevskiy, V. V. Khrustalev, A. L. Mikhailov, M. A. Mochalov, V. Y. Ternovoi, and M. V. Zhernokletov, Phys. Rev. Lett. **99**, 185001 (2007).

[44] M. A. Mochalov, R. I. Il'kaev, V. E. Fortov, A. L. Mikhailov, Y. M. Makarov, V. A. Arinin, S. K. Grishechkin, A. O. Blikov, V. A. Ogorodnikov, A. V. Ryzhkov *et al.*, JETP Lett. **92**, 300 (2010).

[45] G. V. Boriskov, S. I. Belov, A. I. Bykov, M. I. Dolotenko, N. I. Egorov, A. S. Korshunov, Y. B. Kudasov, I. V. Makarov, V. D. Selemir, and A. V. Filippov, J. Low Temp. Phys. **159**, 307 (2010).

[46] M. A. Mochalov, R. I. Il'kaev, V. E. Fortov, A. L. Mikhailov, V. A. Arinin, A. O. Blikov, V. A. Komrakov, I. P. Maksimkin, V. A. Ogorodnikov, and A. V. Ryzhkov, JETP Lett. **107**, 168 (2018).

[47] G. V. Boriskov, A. I. Bykov, N. I. Egorov, M. V. Zhernokletov, V. N. Pavlov, I. S. Strelkov, O. M. Surdin, V. I. Timareva, and S. I. Belov, J. Exp. Theor. Phys. **130**, 183 (2020).

[48] B. Militzer and D. M. Ceperley, Phys. Rev. Lett. **85**, 1890 (2000).

[49] V. S. Filinov, P. R. Levashov, M. Bonitz, and V. E. Fortov, Plasma Phys. Rep. **31**, 700 (2005).

[50] T. Sjostrom and J. Daligault, Phys. Rev. Lett. **113**, 155006 (2014).

[51] R. J. Magyar, L. Shulenburger, and A. D. Baczewski, Contrib. Plasma Phys. **56**, 459 (2016).

[52] A. J. White, O. Certik, Y. H. Ding, S. X. Hu, and L. A. Collins, Phys. Rev. B **98**, 144302 (2018).

[53] V. S. Filinov, V. E. Fortov, M. Bonitz, and P. R. Levashov, JETP Lett. **74**, 384 (2001).

[54] W. Lorenzen, B. Holst, and R. Redmer, Phys. Rev. B **82**, 195107 (2010).

[55] M. A. Morales, C. Pierleoni, and D. M. Ceperley, Phys. Rev. E **81**, 021202 (2010).

[56] G. Mazzola and S. Sorella, Phys. Rev. Lett. **114**, 105701 (2015).

[57] H. Y. Geng, Q. Wu, M. Marqués, and G. J. Ackland, Phys. Rev. B **100**, 134109 (2019).

[58] B. Cheng, G. Mazzola, C. J. Pickard, and M. Ceriotti, Nature (London) **585**, 217 (2020).

[59] G. Mazzola, S. Yunoki, and S. Sorella, Nat. Commun. **5**, 3487 (2014).

[60] J. P. Perdew and A. Zunger, Phys. Rev. B **23**, 5048 (1981).

[61] J.-B. Maillet, E. Bourasseau, L. Soulard, J. Clérouin, and G. Stoltz, Phys. Rev. E **80**, 021135 (2009).

[62] M. A. Paramonov, D. V. Minakov, and P. R. Levashov, J. Phys.: Conf. Ser. **946**, 012089 (2018).

[63] A. V. Chentsov and P. R. Levashov, Contrib. Plasma Phys. **52**, 33 (2012).

[64] D. V. Minakov, P. R. Levashov, K. V. Khishchenko, and V. E. Fortov, J. Appl. Phys. **115**, 223512 (2014).

[65] M. A. Mochalov, R. I. Il'kaev, V. E. Fortov, A. L. Mikhailov, V. A. Arinin, A. O. Blikov, S. E. Elfimov, V. A. Komrakov, V. A. Ogorodnikov, and A. V. Ryzhkov, J. Exp. Theor. Phys. **125**, 948 (2017).

[66] S. I. Blinnikov, R. I. Ilkaev, M. A. Mochalov, A. L. Mikhailov, I. L. Iosilevskiy, A. V. Yudin, S. I. Glazyrin, A. A. Golubev, V. K. Gryaznov, and S. V. Fortova, Phys. Rev. E **99**, 033102 (2019).

[67] M. A. Mochalov, R. I. Il'kayev, V. E. Fortov, S. V. Erunov, V. A. Arinin, A. O. Blikov *et al.*, J. Exp. Theor. Phys. (unpublished).

[68] G. Kresse and J. Furthmüller, Phys. Rev. B **54**, 11169 (1996).

[69] G. Kresse and D. Joubert, Phys. Rev. B **59**, 1758 (1999).

[70] J. P. Perdew, K. Burke, and M. Ernzerhof, Phys. Rev. Lett. **77**, 3865 (1996).

[71] A. Becker, N. Nettelmann, B. Holst, and R. Redmer, Phys. Rev. B **88**, 045122 (2013).

[72] M. A. Mochalov, R. I. Il'kaev, V. E. Fortov, A. L. Mikhailov, Y. M. Makarov, V. A. Arinin, A. O. Blikov, A. Y. Baurin, V. A. Komrakov, V. A. Ogorodnikov *et al.*, J. Exp. Theor. Phys. **115**, 614 (2012).

[73] M. A. Mochalov, R. I. Il'kaev, V. E. Fortov, A. L. Mikhailov, V. A. Raevskii, V. A. Ogorodnikov, A. A. Yukhimchuk, A. I. Davydov, N. N. Anashkin, V. A. Arinin *et al.*, J. Exp. Theor. Phys. **119**, 146 (2014).

[74] M. A. Mochalov, R. I. Il'Kaev, V. E. Fortov, A. L. Mikhailov, A. O. Blikov, V. A. Ogorodnikov, V. K. Gryaznov, and I. L. Iosilevskii, J. Exp. Theor. Phys. **124**, 505 (2017).

[75] G. Kresse and J. Hafner, Phys. Rev. B **47**, 558 (1993).

[76] N. M. Tubman, E. Liberatore, C. Pierleoni, M. Holzmann, and D. M. Ceperley, Phys. Rev. Lett. **115**, 045301 (2015).

[77] S. A. Bonev, B. Militzer, and G. Galli, Phys. Rev. B **69**, 014101 (2004).